Open Access Full Text Article

ORIGINAL RESEARCH

A Multifunctional Nano-Delivery System Against Rheumatoid Arthritis by Combined Phototherapy, Hypoxia-Activated Chemotherapy, and RNA Interference

Xiangyu Li*, Shixin Zhang*, Miaomiao Zhang, Ge Li, Bo Yang, Xinyue Lu, Lesheng Teng 🆔, Youxin Li, Fengying Sun 🆔

School of Life Sciences, Jilin University, Changchun, People's Republic of China

*These authors contributed equally to this work

Correspondence: Fengying Sun, School of Life Sciences, Jilin University, 2699 Qianjin Street, Changchun, Jilin, 130012, People's Republic of China, Tel/Fax +86-431-85155320, Email sunfengying@jlu.edu.cn

Purpose: Effective therapy for rheumatoid arthritis (RA) keeps a challenge due to the complex pathogenesis of RA. It is not enough to completely inhibit the process of RA with any single therapy method. The purpose of the research is to compensate for the insufficiency of monotherapy using multiple treatment regimens with different mechanisms.

Material and Methods: In this study, we developed a new method to synthesize mesoporous silica nanoparticles hybridized with photosensitizer PCPDTBT (HNs). Branched polyethyleneimine-folic acid (PEI-FA) could be coated on the surface of HNs through electrostatic interactions. It simultaneously blocked the hypoxia-activated prodrug tirapazamine loaded into the mesopores and binded with Mcl-1 siRNA (siMcl-1) that interfered with the expression of the anti-apoptotic protein Mcl-1. Released from the co-delivery nanoparticles (PFHNs/TM) Tirapazamine and siMcl-1 upon exposure to acidic conditions of endosomes/lysosomes in activated macrophages. Under NIR irradiation, photothermal therapy and photodynamic therapy derived from PCPDTBT, hypoxia-activated chemotherapy derived from tirapazamine, and RNAi derived from siMcl-1 were used for the combined treatment for RA by killing activated macrophages. PEI-FA-coated PFHNs/TM exhibited activated macrophage-targeting characteristics, thereby enhancing the in vitro and in vivo NIR-induced combined treatment of RA.

Results: The prepared PFHNs/TM have high blood compatibility (far below 5% of hemolysis) and ideal in vitro phototherapy effect while controlling the TPZ release and binding siMcl-1. We prove that PEI-FA-coated PFHNs/TM not only protect the bound siRNA but also are selectively uptaked by activated macrophages through FA receptor-ligand-mediated endocytosis, and effectively silence the target anti-apoptotic protein by siMcl-1 transfection. In vivo, PFHNs/TM have also been revealed to be selectively enriched at the inflammatory site of RA, exhibiting NIR-induced anti-RA efficacy.
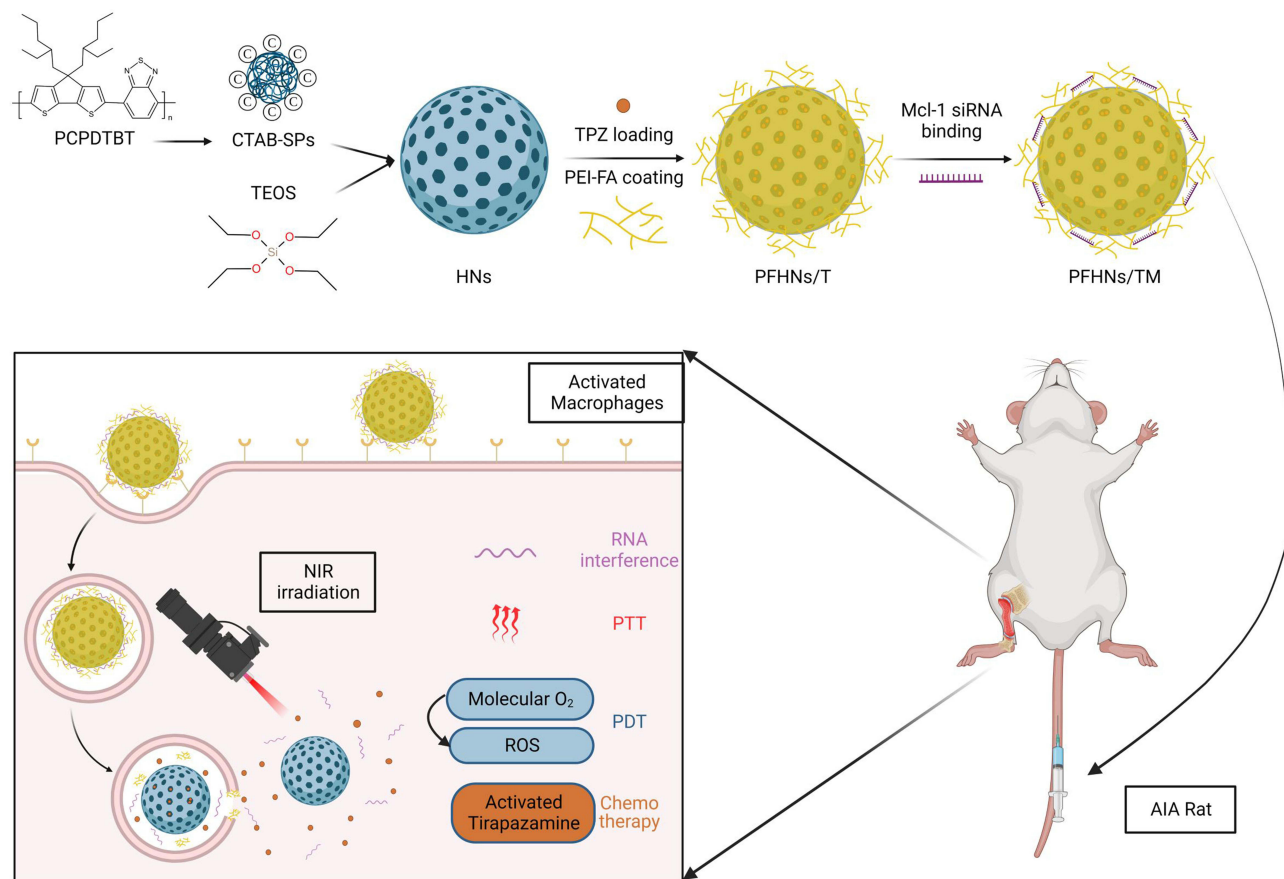
Conclusion: Overall, these FA-functionalized, pH-responsive PFHNs/TM represent a promising platform for the co-delivery of chemical drugs and nucleic acids for the treatment of RA cooperating with NIR-induced phototherapy.

Keywords: rheumatoid arthritis, nano-delivery system, phototherapy, hypoxia-activated chemotherapy, RNA interference

Introduction

Rheumatoid arthritis (RA) is a chronic systemic autoimmune disease that mainly affects the joints.[1] Activated macrophages are deeply involved in the systemic and joint pathologies of RA, including cartilage erosion and bone destruction, by secreting a large number of pro-inflammatory factors and chemokines, which makes them an ideal target for the treatment of RA.[2–4] In addition, a large number of folate receptor-β (FR-β) exists on the surface of activated macrophages. The overexpression of FR-β on the cell surface provides convenience for the targeted delivery of folic acid (FA)

Graphical Abstract

Near-infrared (NIR) induced phototherapy is an effective, non-invasive and mild technique with excellent time-spatial specificity method to kill the target cells, including photodynamic therapy (PDT) and photothermal therapy (PTT).[7–11] Among them, PTT employs a photothermal agent to convert the photon energy from NIR laser into heat energy, causing local overheating to thermally ablate target cells while causing minimal damage to the surrounding normal cells and tissues.[12–14] Unlike PTT, NIR irradiation induces photosensitizers to convert nearby molecular O_2 into cytotoxic ROS (such as singlet oxygen) to destroy target cells, which is defined as PDT.[15] As an emerging material for NIR-induced phototherapy, the semiconducting polymer PCPDTBT with the characteristics of both a photothermal agent and a photosensitizer has been extensively investigated.[16,17] It is obvious that the efficacy of PDT depends on the supply of molecular O_2, and unfortunately, tumors and inflammatory sites are often found to be in a hypoxic microenvironment due to the mismatch between oxygen delivery and consumption, which greatly limits the application of PDT.[18–20] The dual-modal therapy combined with PTT and PDT can appropriately enhance the efficacy of PDT because the local heating caused by appropriate PTT increases the blood flow rate and molecular O_2 supply to the lesion site, which supplements the PDT with raw material for the production of single-linear oxygen in turn.[21] The emergence of hypoxia-activated prodrug tirapazamine (TPZ) provides a way to solve this problem.[22–24] In the local hypoxic microenvironment enhanced by PDT, TPZ can be selectively reduced by specific reductases, generating cytotoxicity to surrounding cells while having little toxicity to normal tissues.

Because of its ability to specifically and reversibly silence target genes, RNA interference (RNAi) caused by small interfering RNA (siRNA) is considered to have the potential to be applied to a variety of diseases.[25,26] The degradation by RNase, potential immune response, and difficulty in diffusion across cell membranes caused by strong anions make the delivery of siRNA remain a huge challenge.[26] Benefiting from the development of nanocarriers, the in vivo delivery of nucleic acid drugs has been realized, among which the delivery technology of siRNA has attracted considerable attention.[27–29] Branched polyethylenimine (PEI) with high cationic charge density, low toxicity and small molecular can bind siRNA to form nano-scale particles, which is an ideal carrier for siRNA. After binding to PEI, siRNA was confirmed to be protected from RNase degradation and was effectively delivered to target cells.[30,31] Myeloid cell leukemia-1 (Mcl-1), as a member of the anti-apoptotic B-cell lymphoma-2 (Bcl-2) protein family, is essential for the survival of macrophages in the joints of RA patients and a potential therapeutic target for the disease.[32] In order to enhance treatment performance and prevent recurrence, it is appealing to combine multimodal therapy within one single nanocarrier for combinational therapy for RA. Silencing of this gene inhibits the expression of the Mcl-1 protein and is able to suppress this escape apoptosis and enhance the killing effect on target cells.

In this study, we report the development of a multifunctional nanocarrier for targeted co-delivery of phototherapeutic agent, chemical drug, and Mcl-1 siRNA (siMcl-1) to kill activated macrophages to treat RA. Due to the high drug loading capacity based on the unique mesoporous structure, mesoporous silica nanoparticles are employed to effectively deliver hydrophobic PCPDTBT to RA lesions. Mesoporous hybrid nanoparticles (HNs) are used for loading of TPZ. FA conjugated PEI (PEI-FA) coated HNs (PFHNs) effectively prevent the leakage of TPZ loaded into the internal mesopores while enhancing the in vitro and in vivo internalization into activated macrophages. It is worth noting that the presence of PEI-FA in PFHNs can compact and bind siRNA for siMcl-1 delivery. Upon NIR irradiation, the hypoxia-activated chemotherapy (HaCT) of TPZ activated by PDT-enhanced hypoxic microenvironment, together with PTT, PDT and RNAi, has a combined cytotoxicity to activated macrophages. We assume that PFHNs co-loading TPZ and siMcl-1 can achieve in vitro and in vivo targeted delivery of phototherapeutic agent, chemical drug, and siRNA, thereby improving the NIR-induced combined RA therapy effect. We verified this assumption in vitro with RAW 264.7 cells activated by lipopolysaccharide (LPS), and then in vivo in a complete Freund's adjuvant-induced arthritis (AIA) rat model.

Materials and Methods

Materials
Cy5-labeled siMcl-1 and siMcl-1 were purchased from RiboBio. PCPDTBT (Sigma-Aldrich, average Mw 7000–20,000), tetrahydrofuran (Sinopharm, analytical reagent grade), Hexadecyl trimethyl ammonium Bromide (CTAB) (aladdin, ≥99.0%), tetraethoxysilane (aladdin, ≥98.0%), branched PEI (Sigma-Aldrich, 1.8 kDa), FA (Shanghai yuanye Bio-Technology Co., Ltd, ≥98.0%), TPZ (Xi'an qiyuebio, ≥98.0%) were used as received.

Synthesis of HNs
HNs were performed via a two-step reaction as we previously reported.[33] First, CTAB-coated SPs (CTAB-SPs) were synthesized by an improved emulsification-solvent evaporation method. Generally, 2 mL PCPDTBT (0.5 mg/mL in tetrahydrofuran) was quickly injected into 8 mL 2% CTAB solution. After 3 min of sonication at 300 W in an ice bath, CTAB-SPs were obtained after evaporating the organic solvent under magnetic stirring at 30°C in the dark. Next, 250 mL ultrapure water was mixed with appropriate amount of obtained CTAB-SPs, 250 mg of CTAB, and 1.4 mL 2 M NaOH, and heated to 80°C. After 20 min, under magnetic stirring at 500 rpm, 2.5 mL tetraethoxysilane was added dropwise (1 mL/min) to the above mixture. After continuous stirring at 80°C for 2 h, HNs were obtained by centrifugation and washed with MeOH three times. The residual CTAB in the mesopores was completely removed by refluxing in MeOH containing hydrochloric acid (16:1, v/v) at 80°C overnight. Subsequently, HNs were collected again by suction filtration and washed with MeOH. The obtained HNs were kept in dark and dry conditions until further use.

Synthesis and Characterization of PEI-FA
PEI-FA was synthesized by forming an amide bond between the carboxylic groups of FA and primary amine groups on PEI. Briefly, 200 mg of FA was dissolved in 10 mL DMSO. Then, 120 mg of EDC and 360 mg of NHS were dissolved in

10 mL DMSO. Subsequently, the above two solutions were mixed in the dark and kept magnetic stirring for 2 h. Next, 30 mL of ultrapure water containing 1400 mg of PEI was added to the above mixture and adjusted to pH 8 with 0.2 M NaOH solution. After being kept stirring in the dark for 3 days, the mixture was transferred to a dialysis bag with ultrapure water to remove residual substances. After 5 days of dialysis, ginger-yellow powder PEI-FA was obtained by freeze-drying. The synthesis of PEI-FA was determined by ultraviolet-visible (UV-Vis) spectrophotometry and Fourier transform infrared spectroscopy (FTIR).

Synthesis of PFHNs and TPZ Loading PFHNs (PFHNs/T)

Briefly, 4 mg of HNs were dispersed in ultrapure water under sonication in the dark, and then appropriate amounts of PEI-FA were added at various weight ratios between HNs and PEI-FA. After 4 h of incubation, PFHNs were obtained by centrifugation (10,000 rpm, 10 min) and washed three times with ultrapure water.

For the preparation of TPZ loaded PFHNs (PFHNs/T), HNs (4 mg) and TPZ were dispersed in ultrapure water under sonication in the dark. After incubation overnight under magnetic stirring, TPZ was loaded into the mesoporous structure of HNs. Subsequently, an appropriate amount of PEI-FA was added in proportion and incubated for another 4 h to block TPZ in the mesopores of HNs. After centrifuged (10,000 rpm, 10 min) and washed with ultrapure water, PFHNs/T was obtained. Free TPZ in the supernatant was measured by UV–vis spectroscopy at 470 nm.

The drug loading (DL) of TPZ in the PFHNs/T was calculated as:

$$\text{DL of TPZ}(\%) = \frac{\text{amount of total TPZ} - \text{amount of free TPZ in the supernatant}}{\text{amount of PFHNs/T}} \times 100\%$$

In vitro pH-Sensitive TPZ Release

The obtained PFHNs/T (3 mg) were suspended in dialysis bags containing 1 mL medium (PBS at pH of 7.4 and 5.0, respectively). The dialysis bags were placed in an additional 9 mL of the medium and incubated at 37°C. At predetermined time intervals, 2 mL of medium was removed for measurement and replaced with 2 mL of fresh medium. The concentrations of TPZ in the medium were analyzed using UV–vis spectroscopy. Three independent experiments were conducted for statistical analysis.

In vitro Photothermal and Photodynamic Properties of PFHNs

To evaluate the NIR power densities-dependent photothermal conversion characteristics of PFHNs, NIR laser at 808 nm at various power densities (0.25, 0.5, 0.75, and 1.0 W/cm^2) was irradiated on the PFHN suspension (300 µL, 1.0 mg/mL in PBS). The effect of PFHN concentration on the heating curve was studied. Various concentrations of PFHN suspension (300 µL, 0.25, 0.5, 1.0 and 2.0 mg/mL in PBS) were irradiated by 1.0 W/cm^2 NIR laser at 808 nm. The NIR-induced heating assay of PFHN suspension (1.0 W/cm^2, 1.0 mg/mL) was performed twice to determine the photothermal conversion stability of PFHNs. The NIR-induced heating curve of the HN suspension (1.0 W/cm^2, 1.0 mg/mL) was also recorded to assess the effect of PEI-FA coating on the photothermal conversion characteristics. Three independent experiments were conducted for statistical analysis.

The in vitro NIR-induced ROS generation properties of PFHNs were determined by DPBF probe. Briefly, 1 mg of PFHNs was added to 0.3 mL of DPBF solution and then irradiated by an 808 nm NIR laser at 1.0 W/cm^2. The $A_{410\ nm}$ of the mixture at predetermined time points was recorded by the microplate reader. Three independent experiments were conducted for statistical analysis.

Agarose Gel Electrophoresis

To determine the binding ability of PFHNs with siRNA, PHFNs and siMcl-1 were mixed at various weight ratios and incubated at room temperature for 2 h to form PFHNs/siMcl-1 (PFHNs/M) complex. Free siMcl-1 of equal concentration was served as control. The agarose gel electrophoresis was conducted in a 1% agarose gel within 1× TAE buffer for 30 min at 120 V.

6260

DovePress

International Journal of Nanomedicine 2022:17

Free siMcl-1 and PFHNs/M were incubated with RNase A, respectively, to determine the protection of PFHNs to siMcl-1. Briefly, 0.2 mL of free siMcl-1 and PFHNs/M (at siMcl-1 concentration, 50 μg/mL) were incubated with 0.1 mL RNase A (30 μg/mL) at 37°C. At predetermined time points (0.5, 1, 2, 4, 8 and 24 h), the incubation was terminated by 30 min of heating at 80°C, and then heparin sodium (2 mg/mL) was used to extract siMcl-1 from PFHNs/M. The methods of electrophoresis and imaging are as described above.

To assess the influence of NIR irradiation and co-delivered TPZ on siRNA, free siMcl-1, PFHNs/M, and PFHNs/TM (at siMcl-1 concentration, 50 μg/mL) were dispersed in DEPC-treated water, respectively, and then irradiated by an 808 nm NIR laser at 1.0 W/cm^2 for 5 min. Subsequently, heparin sodium was used to extract siMcl-1 from PFHNs/M and PFHNs/TM, and electrophoresis and imaging were performed as described above. Unirradiated free siMcl-1, PFHNs/M, and PFHNs/TM were set as control groups.

Characterization

The size and zeta potential of the nanoparticles were determined at 25°C using a Zetasizer (Nano ZS90, Malvern, USA). The distribution of C and Si elements in HNs is visualized by electron energy loss spectroscopy (EELS). The degree of PEI and FA connectivity was assessed by UV–Vis (UV-3150, SHIMADZU, Japan) and FT-IR spectroscopy (IRPrestige-21, SHIMADZU, Japan). The structure of the CTAB-SPs, HNs and PFHNs was observed by transmission electron microscope (TEM) at an accelerating voltage of 200 kV (JEM-F200, JEOL, Japan). The mesoporous properties of nanoparticles were obtained by N_2 adsorption/desorption isotherms (ASAP 2020 plus HD88, Micromeritics, USA). The temperature change of the dispersion was obtained using an infrared thermal camera (C2, Flir, USA). The ROS production was detected by zymography (DNM-9602, Perlong, China). The RNA bands were visualized by GelDoc-It TS™ Imaging Systems (97–0256-02, UVP, USA).

Hemolysis Test

Fresh whole blood was collected from the orbital venous plexus of experimental Sprague-Dawley rats. The red blood cells (RBCs) were obtained by centrifugation (5000 rpm, 4°C, 10 min) and diluted to 2% (v/v) with saline. Different amounts of free siMcl-1 and PFHNs/MD (at siMcl-1 concentration, 0.0125–0.2 nM) were added to 2% RBCs and then incubated at 37°C for 3 h. Triton X-100 and saline were served as the positive and negative controls, respectively.[34] Subsequently, the supernatant obtained by centrifugation was analyzed for the hemolysis rate by a microplate reader at $A_{540 \ nm}$. Three independent experiments were conducted for statistical analysis.

$$\text{Hemolysis ratio}(\%) = \frac{A_{sample} - A_{negative \ control}}{A_{positive \ control} - A_{negative \ control}} \times 100\%$$

Cell Culture

Unactivated RAW 264.7 cells (Procell, China) were cultured in DMEM supplemented with 10% FBS at 37°C in a humidified atmosphere of 5% CO_2. RAW 264.7 cells cultured in DMEM supplemented with 10% FBS and LPS (1 μg/mL) were served as activated macrophage model.

Cellular Uptake Assay

Activated RAW 264.7 cells (2×10^5 cells/well) were incubated overnight and then cultured with Cy5-labeled PFHNs/M, Cy5-labeled PHNs/M, Cy5-labeled PFHNs/M (cells were pre-treated with excess FA for 4 h), and free Cy5-labeled siMcl-1 for 4 h. Subsequently, the cells were washed to remove residual nanoparticles and fixed with 2% (w/v) glutaraldehyde. Then, the cellular nuclei were stained with DAPI. Unactivated RAW 264.7 cells treated with the same conditions were served as a control group. Cellular uptake of different nanoparticles was observed by confocal laser scanning microscope (CLSM).

To quantitatively measure the time-dependent cellular uptake of nanoparticles, flow cytometry analysis was performed. Briefly, activated RAW 264.7 cells were seeded in 6-well at a density of 2×10^5 cells/well and incubated for 24 h. Then the cells were washed with PBS and cultured with Cy5-labeled PFHNs/M and Cy5-labeled PHNs/M at

predetermined time points (0.5 h, 1 h, 2 h, 4 h). After that, the treated cells were washed three times with pre-cooled PBS to remove residual nanoparticles. Subsequently, in 1 mL of pre-cooled PBS, the cells were collected by a cell scraper and filtered into a flow tube. Cellular uptake was analyzed using flow cytometry (EPICS XL). FACS data were collected using CytExpert Software and analyzed by FlowJo for fluorescence quantification.

NIR-Induced Intracellular Hypoxia/Singlet Oxygen Detection

Activated RAW 264.7 cells were seeded in 12-well at a density of 2×10^5 cells/well and incubated overnight. After washing three times with PBS, the cells were cultured with PFHNs for 4 h. The cells were washed again and irradiated by an 808 nm NIR laser at 1.0 W/cm^2 for 5 min. Immediately, the NIR-induced ROS was stained with DCFH-DA. Similarly, the NIR-induced intracellular hypoxia was detected by Hypoxyprobe-1™ kit according to the manufacturer's instructions, and the fluorescence of FITC in treated cells was visualized by CLSM.

Western Blot Analysis

Activated RAW 264.7 cells were seeded in 6-well at a density of 2×10^6 cells/well followed by stabilization overnight and treated with free siMcl-1, PHNs/M and PFHNs/M and then lysed in 200 μL RIPA buffer containing 1% sodium orthovanadate and 1% phenylmethylsulfonyl fluoride in an ice bath for 30 min. The lysate was then collected by centrifugation (12,000 rpm, 4°C, 10 min). Subsequently, the protein concentration was determined by the BCA assay. Protein samples (20 μL) were electrophoresed on a 10% sodium dodecyl sulfate-polyacrylamide gel electrophoresis (SDS-PAGE) and transferred to a polyvinylidene difluoride (PVDF) membrane. After 2 h of blocking (blocking solution containing 5% skim milk), the membrane was incubated with anti-Mcl-1 antibody (1:1000) or β-Tubulin (1:1000) overnight. The PVDF membrane was washed with tris-buffered saline with Tween-20 three times and incubated with a secondary goat anti-rabbit antibody. Protein bands were detected by the ECL kit and visualized by chemiluminescent imaging system (5200, Tanon, China).

Evaluation of Cell Viability by MTT Assay

Cell viability was evaluated as previously described.[33] Briefly, activated and unactivated RAW 264.7 cells were seeded in 96-well at a density of 1×10^4 cells/well and incubated for 24 h. Subsequently, the cells were washed with PBS and cultured with free TPZ, PFHNs, PFHNs/T, PFHNs/M and PFHNs/TM at various TPZ concentrations, respectively. After incubation for 4 h, the cells were washed with PBS to remove residual nanoparticles, and then irradiated by an 808 nm NIR laser at 1.0 W/cm^2 for 5 min. Cell viability was analyzed by MTT assay and calculated as:

$$\text{Cell viability} = \frac{A_{sample} - A_{blank}}{A_{negative\ control} - A_{blank}} \times 100\%$$

The unirradiated cell viability was assayed under the same conditions.

Establishment of AIA Rat Model

Male Sprague-Dawley rats (160–180 g) were obtained from Liaoning Changsheng Biotechnology Co., Ltd. All animal experimental protocols were approved by the Institutional Animal Care and Use Committee of Jilin University (Number of permit: SY202111027). Animal care was following the Laboratory Animals-Guidelines for ethical review of animal welfare in China (GB/T 35892–2018). All the rats were fed with a chlorophyll-free chow before the experiment.

Complete Freund adjuvant (CFA) containing 10 mg/mL of heat-killed *Mycobacterium tuberculosis* was obtained from Chondrex, Inc. According to the protocol for AIA rat model, 50 μL of CFA was subcutaneously injected into the left footpads of the rats. On day 4 after CFA injection, severe and acute inflammation of the joints was observed, and continued to develop thereafter. On day 14 after CFA induction, AIA rat model was successfully induced. During this process, the severity of arthritis in rats was assessed every two days by clinical scores of the joint swelling severity and thickness of the hind paws. The arthritis severity of the rats was scored as follows: 0 = no erythema or swelling, 1 = slight swelling and confined erythema, 2 = slight swelling and extended erythema, 3 = moderate swelling and extended erythema, 4 = severe swelling and widespread erythema.

In vivo Biodistribution

Free Cy5-labeled siMcl-1, Cy5-labeled PHNs/TM and Cy5-labeled PFHNs/TM were intravenously injected by tail vein into AIA rats (at a siMcl-1 concentration of 10 nm/kg). At predetermined time points, the rats were euthanized; then, the joints and major organs were collected for fluorescence imaging using IVIS spectrum (Caliper Life Sciences; Ex/Em = 605/660 nm).

In vivo Therapeutic Efficacy

On day 14 after CFA induction, the rats were randomly divided into seven groups denoted as Control, AIA, PFHNs/TM +L, PFHNs/T+L, PHNs/TM+L, PFHNs/TM and PFHNs+L, where "L" means irradiated by NIR laser. All the nano-particles were intravenously injected (at siMcl-1 concentration of 10 nM/kg or equal dose of nanoparticles), and the injection volume is 0.4 mL. Rats in the AIA group were intravenously injected with saline. After 30 min, the inflammatory joints from the laser-irradiated group were exposed to an 808 nm NIR laser at 1.0 W/cm^2 for 5 min. Related assessments were conducted on days 14, 15 and 17.

Radiological Examination and Histological Analysis

All the rats were euthanized on day 17. The ankle joints were harvested, and diagnosed joint damage was evaluated by X-rays. For histological analysis, the obtained ankle joints were fixed in 4% formaldehyde and then decalcified for three months. Subsequently, the fixed ankle joints were embedded in paraffin, sectioned, and stained with hematoxylin and eosin (H&E). The stained sections were observed under a microscope (Olympus, Tokyo, Japan).

Cytokine Detection

On day 17 after CFA induction, ankle joints and serum of experimental rats were obtained, and the levels of pro-inflammatory cytokines (TNF-α, IL-1β, and IL-6) and anti-inflammatory cytokines (IL-10) in inflamed joints and in serum were detected by ELISA kits and immunohistochemical analysis.

In vivo Biosafety Assessment

During the development of the AIA rat model and treatment process, the weights of experimental rats were recorded. On day 17 after CFA induction, major organs (heart, liver, spleen, lung, and kidney) were harvested, for histopathological examination.

Statistical Analysis

The data were expressed as mean ± standard deviation (SD). Statistical significance was determined using a one-way analysis of variance. Statistical significance was assigned as $*p < 0.05$, $**p < 0.01$, and $***p < 0.001$. Statistical significance was set at $p < 0.05$.

Results and Discussion

Synthesis and Characterization of HNs

For HN synthesis, using CTAB as an emulsifier and PCPDTBT as a photosensitizer, nano-scale quantum dots CTAB-SPs were obtained under ultrasound. CTAB on the surface of SPs was also functioned as a template to generate mesoporous silicon structure, and thereby, HNs were obtained. As shown in Figure 1A, CTAB-SPs had a uniform distribution at an average particle size of 4.85 ± 0.65 nm. The PDI was shown in Table S1. Figure 1B shows that CTAB-SPs exhibited irregular shapes and monodispersity. The TEM image exhibited that HNs were approximately spherical and had a highly ordered mesoporous structure, which was conducive to subsequent drug loading, as shown in Figure 1C. According to the EELS results (Figure 1D–F) of HNs, C element from PCPDTBT and the Si element from mesoporous silicon exhibited co-localization, indicating that SPs were evenly distributed inside HNs and well hybridized with mesoporous silicon, which was beneficial to exert their photosensitive properties.
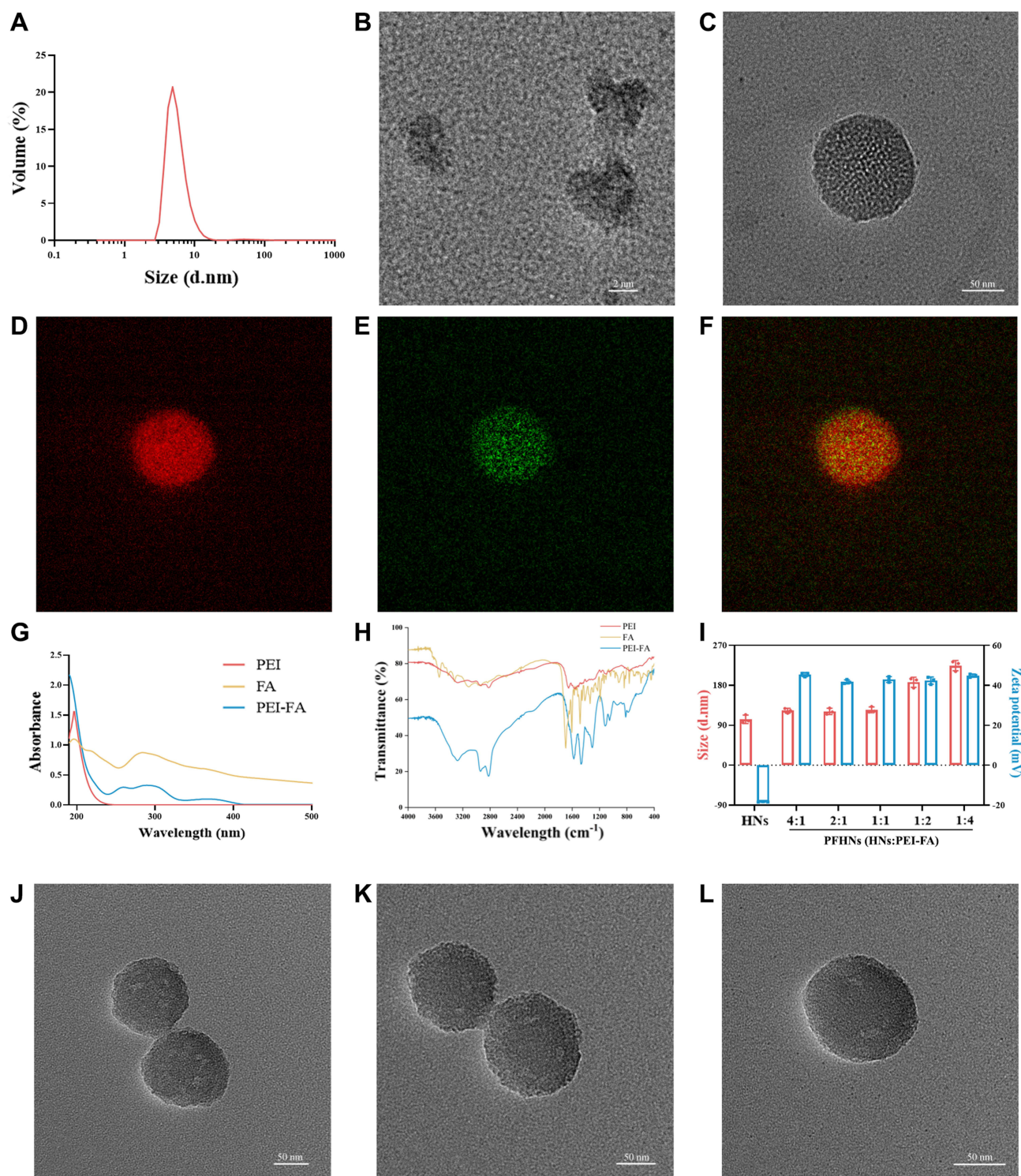
Figure 1 (**A**) Particle size distribution of CTAB-SPS. Representative TEM images of CTAB-SPS (**B**) and HNs (**C**). Representative EELS images of the distribution of C (**D**) and Si (**E**) elements in HNs and their co-localization (**F**). UV-vis (**G**) and FTIR (**H**) spectra and of PEI, FA, and PEI-FA. (**I**) The particle size and zeta potential of HNs and PFHNs (at various weight ratios between HNs and PEI-FA, n = 3). Representative TEM images of PFHNs at weight ratios between HNs and PEI-FA of 4:1 (**J**), 2:1 (**K**), and 1:1 (**L**).

Characterization of PEI-FA

HNs were then coated with a layer of PEI-FA to block the mesoporous pores and prevent the loaded drugs from leakage. PEI-FA was selected as the coating for a variety of other reasons, including the biocompatibility of low molecular weight PEI (1.8 kDa), the targeting ability of FA molecules to activate macrophages, and its strong positive charge for subsequent delivery of

siRNA. Before that, PEI-FA was synthesized. UV-Vis and FTIR analyses were conducted for the characterization of PEI-FA. In UV–Vis analysis (Figure 1G), the spectrum of PEI-FA exhibited the characteristic peaks of PEI and FA (starting material) spectra. The conjugation of FA with PEI was conducted by activating FA with EDC/NHS, as shown in Figure 1H, the presence of a strong new peak at 1620 cm^{-1} attributed to stretching of amide, indicating the chemical conjugation of FA with PEI.

Synthesis and Characterization of PFHNs

The weight ratio of PEI-FA and HNs was adjusted to obtain a suitable coating layer. As shown in Figure 1I, HNs exhibited a uniform distribution (further confirmed by PDI data in Table S1) with an average particle size of 103.37 ± 9.51 nm and a zeta potential of -18.37 ± 0.15 mV. When the weight ratio between HNs and PEI-FA was greater than 1, PFHNs exhibited a strong positive charge with ideal particle size. As the weight ratio of PEI-FA increased, the particle size of PFHNs increased significantly and showed poor dispersibility, which was not suitable for intravenous administration. PFHNs with suitable weight ratios between HNs and PEI-FA (4:1, 2:1 and 1:1) were selected for further research. TEM images (Figure 1J–L) showed that, compared with HNs, the PEI-FA layer coating on PFHNs was observed. And with the increase in the weight ratio of PEI-FA, the trend of more complete layer coating of HNs was obviously observed. Theoretically, the completeness of the PEI-FA coating layer is vital for blocking mesopores and the controlled release of drugs.

TPZ Loading and in vitro pH-Sensitive Release

The weight ratio between HNs and PEI-FA was finally determined according to the drug loading and in vitro release characteristics of PFHNs/T. As shown in Figure 2A, the DL of TPZ in PFHNs/T with various weight ratios between HNs and PEI-FA (4:1, 2:1, and 1:1) were calculated to be $10.85 \pm 0.31\%$, $8.08 \pm 0.21\%$, and $6.02 \pm 0.08\%$, respectively.

As shown in Figure 2B, all PFHNs/T formulations are rapidly released in the medium at pH 5.0, and the loaded TPZ is almost completely released within 4 h. This could be attributed to the protonation of the amine group. PEI-FA was positively charged under acidic conditions and generated strong electric repulsion with HNs, which led to the dissociation of the PEI-FA coating layer and unblocking of the mesoporous pores. On the contrary, at neutral pH, PEI-FA with strong
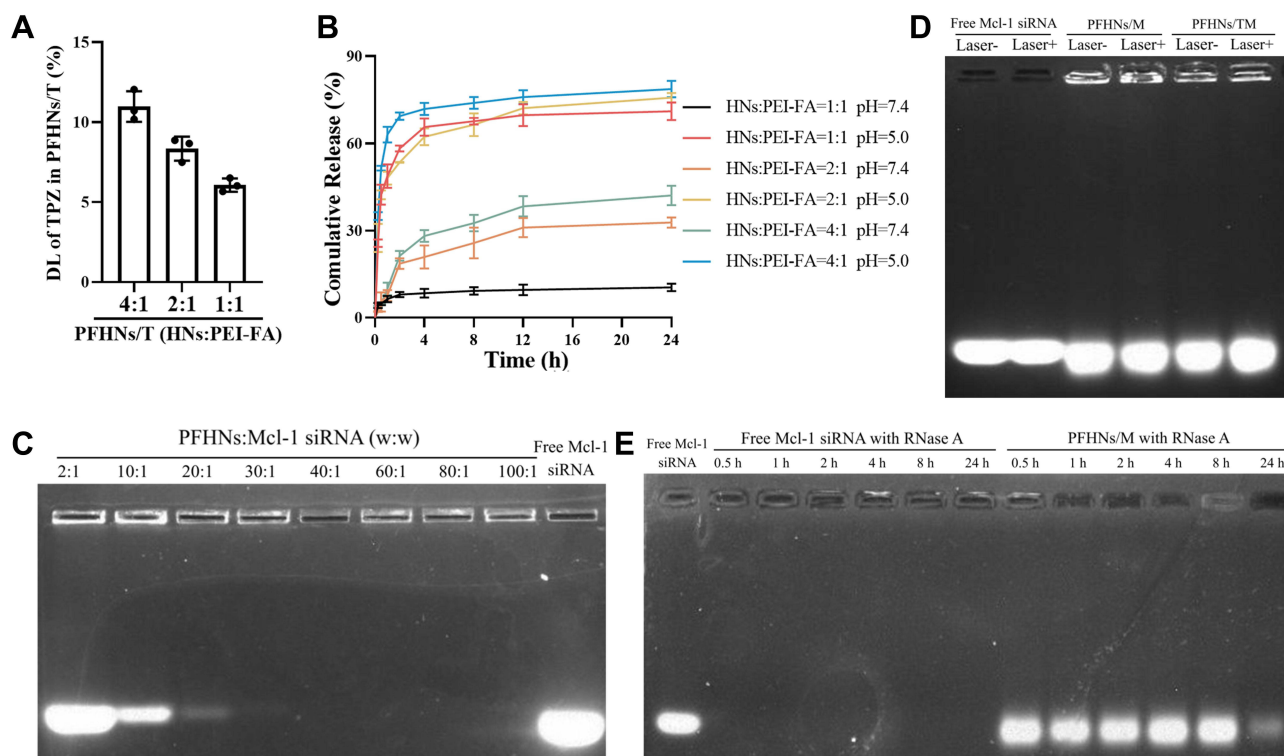

Figure 2 (**A**) Effect of HNs/PEI-FA ratio on the loading capacity of PFHNs/T. (**B**) Effect of HNs/PEI-FA ratio on in vitro release of PFHNs/T. (**C**) Agarose gel electrophoresis of PFHNs/M at various w/w ratios between PFHNs and siMcl-1. (**D**) Effect of NIR irradiation and co-delivered TPZ on siMcl-1 from PFHNs/M and PFHNs/TM. (**E**) Protection of PFHNs/M to siMcl-1 against RNase A (n = 3).

positive charge tightly coated the surface of HNs and blocked the mesoporous pores to prevent the leakage of TPZ. Among them, when PEI-FA was insufficient (weight ratios HNs:PEI-FA of 4:1 and 2:1), the 24-h cumulative-release amounts of TPZ from PFHNs/T were 42.08 ± 3.35% and 32.78 ± 1.78%, respectively. Notably, the 24-h cumulative release of TPZ from PFHNs/T (weight ratio HNs: PEI-FA of 1:1) was extremely low at 10.42 ± 1.30%, which indicated that the PEI-FA coating layer of this formulation was more complete, even with a relatively lower DL, and more TPZ could be delivered to the inflammatory lesion. Therefore, the formulation of PFHNs/T (weight ratio HNs:PEI-FA of 1:1) was determined for further use.

In vitro Photothermal and Photodynamic Properties

The photothermal conversion efficiency of the nanoparticles was evaluated by monitoring the heating profiles of suspension under NIR irradiation. As illustrated in Figure S1A, under the 808 nm NIR irradiation, the temperature of the PFHN suspension increased with the irradiation time and exhibited power density-dependence of NIR laser. Considering patient tolerance and PTT effect, NIR laser at 1.0 W/cm^2 was selected for follow-up research, and the irradiation time was set to 5 min. The temperature change (ΔT) of the suspension under an NIR irradiation at 1.0 W/cm^2 was found to be positively related to the concentration of PFHNs (Figure S1B). The photothermal stability of PFHNs under NIR laser was conducted in a two-cycle photothermal conversion. As shown in Figure S1C, the approximately overlapped profiles of the two-cycle photothermal conversion indicated that the photothermal conversion efficiency of PFHNs had no degradation. Figure S1D showed that the ΔT of PBS (suspended medium) within 5 min was determined to be 4.43 ± 0.58°C, while the ΔT of HNs and PFHNs within 5 min were 35.37 ± 0.50°C and 33.80 ± 0.26°C, respectively, denoting that the PEI-FA coating was irrelevant to the photothermal conversion efficiency of the formulation. This improves the targeting ability without affecting the photothermal properties of the nanoparticles.

As an approved ROS probe, DPBF could be oxidized by ROS, resulting in its absorption at 410 nm decreased irreversibly, and thus, it was picked to monitor the in vitro NIR-induced ROS generation by PFHNs. As exhibited in Figure S1E, under 180 s of NIR laser irradiation, DPBF was completely oxidized by ROS generated by PFHNs, which proves the NIR-induced PDT effect of PFHNs. Noteworthy, the hypoxic microenvironment generated by the consumption of molecular O$_2$ of NIR-induced PDT was essential for activating the cytotoxicity of TPZ.

Agarose Gel Electrophoresis Assay

The binding capacity between siMcl-1 and PFHNs was determined using a gel electrophoresis assay. Figure 2C shows that when the weight ratio between PFHNs and siMcl-1 increases to 30:1, almost all siRNA was bound with the cationic particle surface of PFHNs. Nanoparticles were not able to enter the gel due to their size. The extra RNA that was not electrostatically adsorbed by the nanoparticles was shown in agarose gel electrophoresis after different ratios of input siRNA. As illustrated in Figure 2D, the bound siMcl-1 was obvious independent of NIR irradiation and co-delivered TPZ. In addition, the protection by PEI-FA of siRNA against RNase A had also been confirmed. As shown in Figure 2E, after incubating with RNase A for up to 8 h, the protected siMcl-1 extracted from PFHNs/M remained undegraded, while the naked siMcl-1 as control was completely degraded by RNase A within 0.5 h. Based on the above results, we have settled on a formulation of PFHNs/TM with weight ratios between HNs and PEI-FA of 1:1 and between PFHNs and siMcl-1 of 30:1 for subsequent research.

Characterization of Porous Structure

The porous structure characteristics of the formulations were carried out by N$_2$ adsorption/desorption assay. As shown in Figure S2A–C, only HNs exhibited standard Type IV isotherms, indicating the presence of a mesoporous structure conducive to favorable drug loading capacity. After PEI-FA coating, the mesoporous structure of PFHNs was completely blocked to prevent the loaded drug from leaking. In addition, the TPZ loading and the electrostatic binding between siMcl-1 and PEI-FA could not detach the PEI-FA from HNs. The mean pore size of HNs was detected as 3.53 nm (Figure S2D). Since CTAB is a template for mesoporous structures, the detected pore size does not differ much from the size of CTAB-NPs. The surface area and Barrett–Joyner–Halenda (BJH) pore volume of HNs calculated from N$_2$ adsorption/

desorption isotherms were 1074.34 m^2g^{-1} and 1.16 cm^3g^{-1}, respectively. The corresponding parameters of PFHNs (57.40 m^2g^{-1} and 0.33 cm^3g^{-1}) and PFHNs/TM (45.23 m^2g^{-1}, and 0.27 cm^3g^{-1}) were determined, respectively.

Hemolysis Assay

Hemolysis was a simple and vital index to assess the blood compatibility of the obtained formulations. No hemolysis was observed even incubating with high concentrations of free siMcl-1 and PFHNs/M. The hemolysis rate of all treated groups was less than 5% which was regarded as the standard, indicating that PFHNs/TM had good blood compatibility and was suitable for intravenous injection (Figure S3). The result showed the safety of the nano-delivery system we designed to some extent.

Cellular Uptake Assay

The cellular uptake assays of the obtained formulations were carried out on activated and unactivated macrophage models. LPS-activated RAW 264.7 cells were cultured with Cy5-labeled PFHNs/M, Cy5-labeled PHNs/M, and free Cy5-labeled siMcl-1. Subsequent CLSM results (Figure 3A) showed that weak fluorescence signals were observed in all the unactivated macrophage groups. Strong fluorescence signals were observed in the cytoplasm of Cy5-labeled PFHNs/M-treated activated RAW 264.7 cells, while the fluorescence signals of Cy5-labeled PHNs/M and free Cy5-labeled siMcl-1 treated groups were obviously weaker, indicating that PEI-FA-coated formulation could be internalized into activated macrophages that overexpressed FA receptors. To determine whether the FA-functionalized formulation was selectively internalized into activated macrophages overexpressing FA receptors through receptor-mediated endocytosis, cells were pretreated with excess free FA before incubating with Cy5-labeled PFHNs/M to block all FA receptors overexpressed on the cell surface. Notably, the fluorescence signal of Cy5-labeled PFHNs/M was observed to be diminished in cells pretreated with excess FA, which indicates that PFHNs/M are indeed internalized into activated macrophages mainly through FA receptor-mediated endocytosis.

Similar results were also displayed by flow cytometry results (Figure 3B–D) corroborating the CLSM results. For activated RAW 264.7 cells, FA-functionalized PFHNs/M had a stronger internalization ability than PHNs/M, and the MFI at 4 h was determined to be approximately 2.27 times that of the PHNs/M treated group. Effective internalization into activated macrophages was the basis for combined therapeutic of PFHNs/TM. In fact, the uptake results shown in Figure 3C were less time-dependent compared to the non-targeted group, so that folic acid was more of an uptake efficiency than an additive capacity.

Intracellular ROS and Hypoxia Detection

After confirming effective cellular uptake and internalization pathways, the detection of NIR-induced intracellular ROS and hypoxic microenvironment generation were performed. As shown in Figure 3E and F, no relevant fluorescent signal was detected in the unirradiated groups. Under NIR irradiation, strong DCF and FITC fluorescence signals were observed in the cytoplasm of activated macrophages, indicating that the internalized PFHNs generated ROS and hypoxic microenvironment. A large amount of molecular O_2 is converted into ROS under NIR irradiation by PCPDTBT. This depletion of the intracellular dissolved oxygen, was believed to be the cause of the generation of the intracellular hypoxic microenvironment. The cytotoxicity of TPZ was then activated by the generated hypoxic microenvironment, to induce free radical-mediated oxidative DNA damage and kill activated macrophages.

Western Blot Assay

Inhibition of the expression of the anti-apoptotic protein Mcl-1 was the precondition for combined therapy. To verify the silence of Mcl-1, Western blot assay was performed. In this assay, β-tubulin was selected as the internal standard protein to standardize the analysis of the target protein. As shown in Figure 3G, the gray value of the protein bands derived from the lysate of PFHNs/M-treated cells significantly decreased. The expression of Mcl-1 protein in the free siMcl-1 and PFHNs/M treated groups was 58.85 ± 9.57% and 37.65 ± 5.04% of the control group, respectively. These quantitative results indicated that free siMcl-1 was effective in silencing Mcl-1, while a more obvious transfection efficiency was
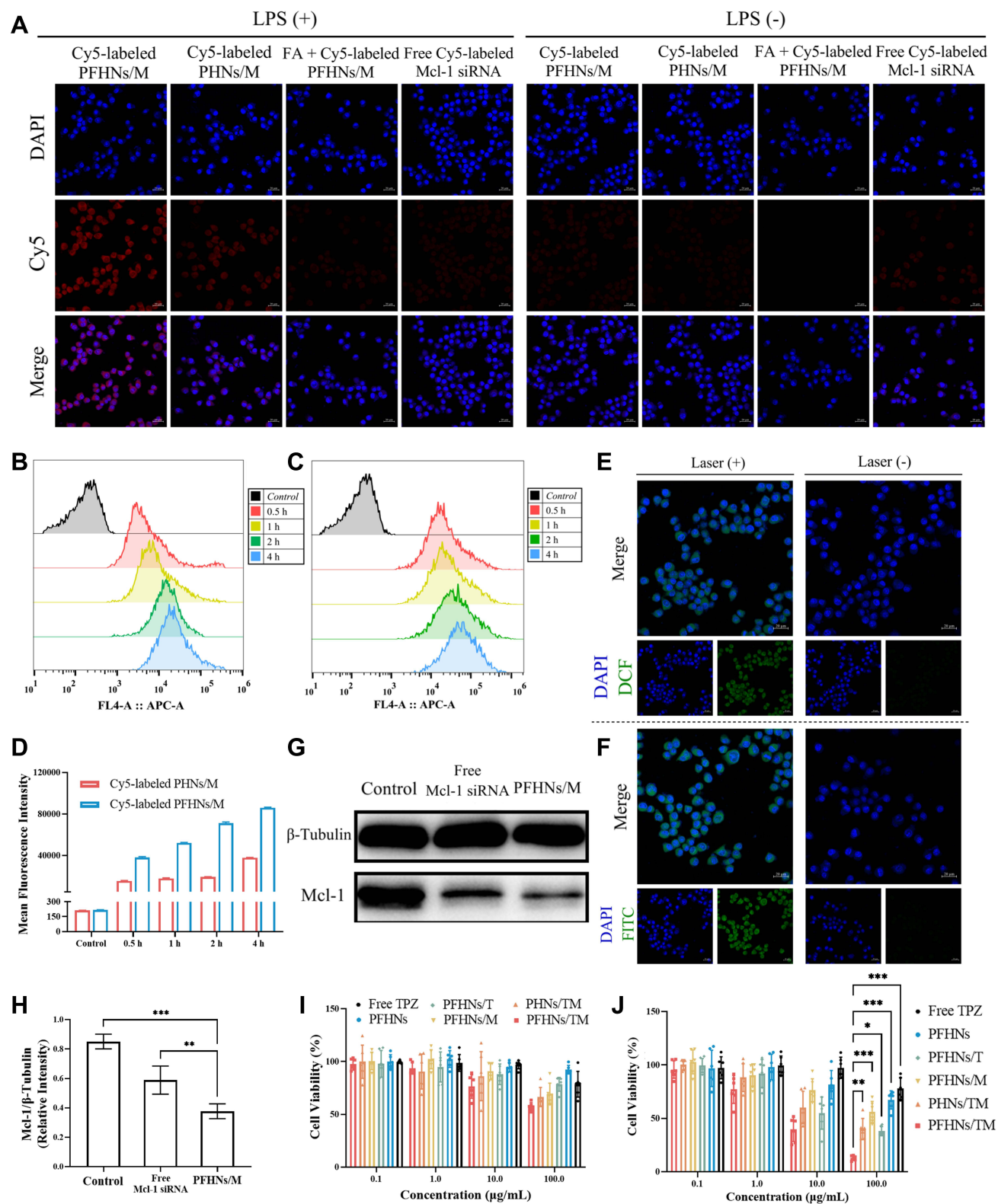
Figure 3 (**A**) Cellular uptake of different formulations by activated (LPS+) and unactivated (LPS-) RAW 264.7 cells. Internalization of PHNs/M (**B**) and PFHNs/M (**C**) by activated RAW 264.7 cells through flow cytometry analysis. (**D**) Mean fluorescence intensity derived from flow cytometry analysis. NIR-induced ROS (**E**) and hypoxia (**F**) generation by PFHNs in activated RAW 264.7 cells. (**G**) Western blot analysis of Mcl-1 protein expression in activated RAW 264.7 cells treated by PBS, free siMcl-1 and PFHNs/M. (**H**) Relative intensity (defined as the intensity of the Mcl-1 protein normalized to β-Tubulin). Cell viability of activated RAW 264.7 cells treated with different formulations (**I**) without and (**J**) with NIR irradiation. (Data are expressed as means ± SD (n = 6). Statistical significances were calculated via ANOVA, *p < 0.05, **p < 0.01, and ***p < 0.001).

determined in the PFHNs/M treated group (Figure 3H), which could be explained by differences in cellular uptake assay, that was FA-functionalized PFHNs were beneficial for the transfection of siRNA into activated macrophages.

Cytotoxicity

Based on the effective internalization into activated macrophages, NIR-induced intracellular generation of ROS and hypoxic microenvironment, and the silence of the anti-apoptotic protein Mcl-1, combined cytotoxicity of PFHNs/TM against activated macrophages, was expected. Cytotoxicity of the obtained formulations was then evaluated by cell viability calculated from MTT assay. All experimental groups were performed independently with/without NIR irradiation. As shown in Figure 3I and J, without NIR irradiation, the viability of the high-concentration PFHNs treated cells was close to 100%, indicating the good biocompatibility. The cell viability of the free TPZ and PFHNs/T (at 100 μg/mL TPZ concentration) treated groups in the oxygen-enriched microenvironment remained to be more than 75%. The cytotoxicity of the PFHNs/M treated group was attributed to the silence of Mcl-1 protein resulting from the transfection of siMcl-1. Many research findings revealed that oxidative stress may induce apoptosis. The cytotoxicity of PFHNs/TM was found to be stronger than that of PHNs/TM at the same TPZ concentration, which was the manifestation of the enhanced internalization mediated by FA functionalization. All experimental groups irradiated by NIR were detected strongly concentration-dependent cytotoxicity. The difference in cytotoxicity of the PFHNs treated groups with or without NIR irradiation was attributed to the NIR-induced PTT and PDT effects. Due to the NIR-induced hypoxic microenvironment, the cytotoxicity of PFHNs/T, PHNs/TM and PFHNs/TM was enhanced to varying degrees. Among them, at high concentration treatment, the NIR-induced cytotoxicity of PFHNs/TM was significantly stronger than that of other experimental groups. This high toxicity was attributed to the high sensitivity of RAW264.7 cells after siMcl-1 silencing. Up to this, the anti-apoptotic effect of Mcl-1 could be removed, and the effect of our chemotherapy and PDT-induced apoptosis could be enhanced to some extent. The targeted combined killing cytotoxicity of PFHNs/TM induced by NIR irradiation was proved by the above results.

In vivo Biodistribution

The targeting strategy of FA functionalization to activated macrophages was evaluated by intravenously delivering three different formulations (free Cy5-labeled siMcl-1, Cy5-labeled PHNs/TM and Cy5-labeled PFHNs/TM) to AIA rats. In vivo biodistribution images of the harvested organs/joints were displayed (Figure 4A and B) at 0.5 and 24 h postinjection of the nanoparticles. The 0.5 h image results showed that the fluorescence intensity of the organs/joints from free Cy5-labeled siMcl-1 treated group was hardly observed, which was attributed to the in vivo degradation of RNase. The biodistribution results of FA functionalized formulation were basically the same as those of non-functionalized formulation, that is, strong fluorescence was observed in kidneys and inflammatory joints. Noteworthy, due to the FA functionalization, obviously stronger fluorescence accumulation was shown in the inflammatory joints from the PFHNs/TM treated group, which was 1.86 times of the PHNs/TM treatment group. For the 24 h images, only negligible fluorescence accumulation was observed in the inflammatory joints from all treated groups, indicating the fast excretion. These results indicated that FA-functionalized PFHNs/TM by systemic administration basically preferentially accumulated in RA joints in vivo.

In vivo NIR-Induced Treatment

The excellent targeted biodistribution and the NIR-induced combined cytotoxicity of PFHNs were expected to provide a safe and effective treatment for RA. AIA rat model was selected to assess the in vivo efficacy in suppressing RA. As shown in Figure 4C, on day 14 after CFA induction, the AIA rat model was established, and two treatments were performed once every two days (day 14 and 16). The therapy of each treated group was evaluated by recording the changes of inflammatory joints, including paw thickness and clinical score. On day 17, relatively moderate relief of RA clinical symptoms were observed from the rats in PFHNs/T+L, PHNs/TM+L, PFHNs/TM and PFHNs/L treated groups, and their mean clinical scores were determined to be 2.33 ± 0.52, 2.50 ± 0.84, 3.00 ± 0.75 and 2.67 ± 0.82, respectively, while the clinical score of AIA group rats with severe swelling and erythema was 3.50 ± 0.84 (Figure 4D). Consistent results were recorded in paw thickness evaluation (Figure 4E). Different degrees of reduction in paw thickness of AIA rats were observed in the above-mentioned treated groups, but the progression of RA could not be completely inhibited. In contrast, the effect of targeted NIR-induced
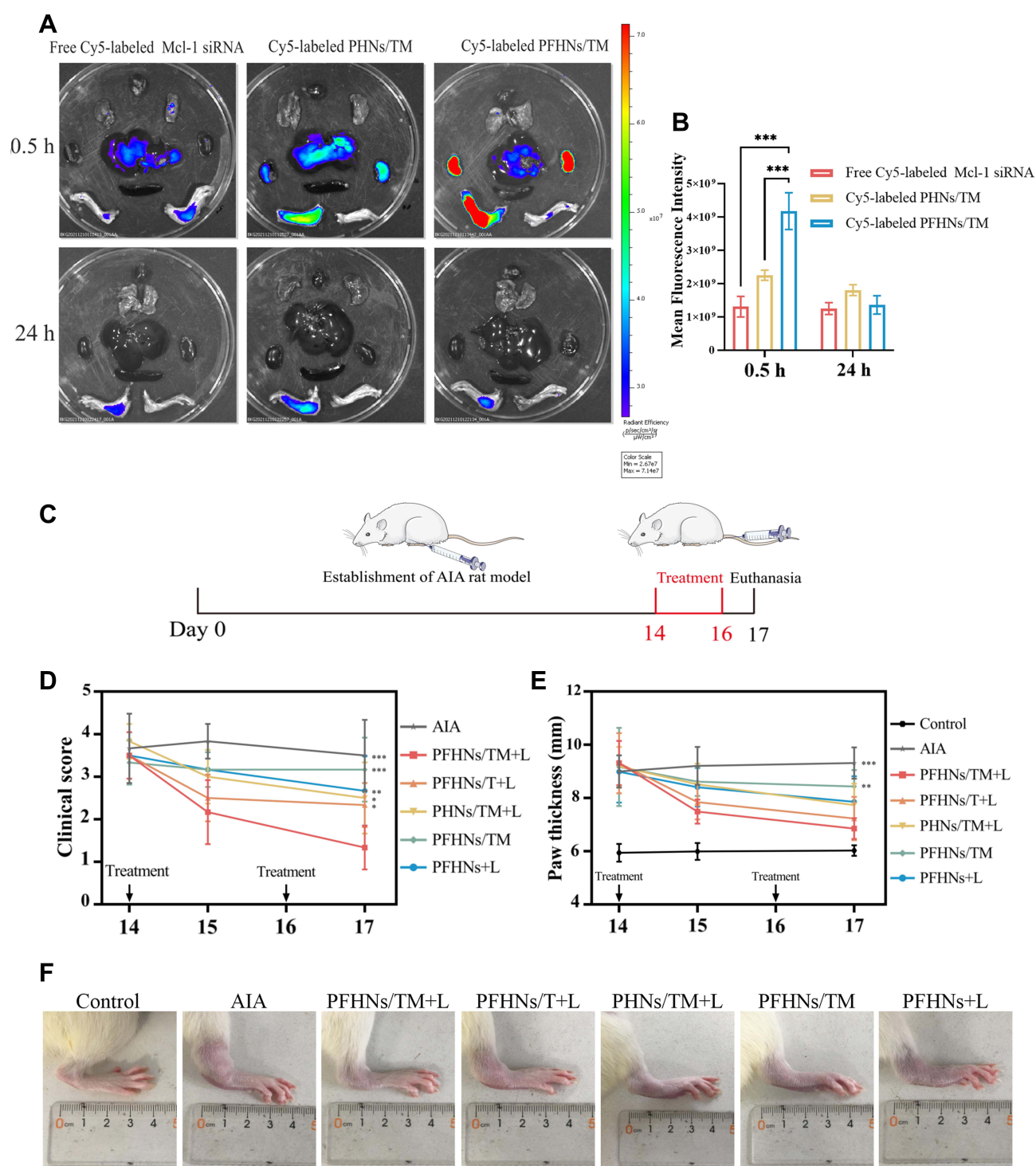
Figure 4 In vivo biodistribution (**A**) and mean fluorescence intensity of inflamed joints (**B**) in AIA rats treated with free Cy5-labeled siMcl-1, Cy5-labeled PHNs/TM, Cy5-labeled PFHNs/TM. (**C**) AIA rat model establishment and in vivo treatment scheme. (**D**) Clinical score and (**E**) paw thickness change curves after treatment (n=6). (**F**) Representative photographs of inflamed ankle joints on day 17 from different groups. (***$p < 0.001$.)

combined therapy (PTT+PDT+HaCT+RNAi) was confirmed in the PFHNs/TM+L treated group, and the average clinical score and paw thickness were determined to be 1.33 ± 0.52 and 6.70 ± 0.39 mm, respectively, which were the closest to the control group. Figure 4F also shows that the swelling and erythema of inflamed ankle joints from PFHNs/TM+L treated group were significantly relieved on day 17, indicating a strong potential therapeutic efficacy in RA.

Delightful results were also found in X-rays diagnosis and histological analysis results. For X-ray diagnosis (Figure S4), the joints of AIA rats were found to be markedly swollen, accompanied by marginal bone hyperplasia, while the edema of the periarticular soft tissue from rats treated with PFHNs/TM+L was found to be the most obviously relieved.

Consistent remission of inflammation was found in H&E staining results of inflamed joints. As shown in Figure 5A, the synovial tissue structure of AIA rats was disorganized, accompanied by severe fibrous tissue hyperplasia and inflammatory cell infiltration (at the black arrow). After treatment, only the rats from PFHNs/TM+L group had normalized joint structure with smooth cartilage surface and neatly arranged chondrocytes.

Imbalance in the secretion of pro-inflammatory cytokines (TNF-α, IL-1β, and IL-6) and anti-inflammatory cytokine (IL-10) leads to worsening of inflammation. As shown in Figure 5B–F, the levels of pro-inflammatory cytokine in inflamed joints and serum from AIA rats were obviously higher than those of the control group, and pro-inflammatory cytokine levels decreased to different degrees in all treated groups of rats, among which the PFHNs/TM+L treated group was the closest to the normal level. Unlike pro-inflammatory cytokines, the level of anti-inflammatory cytokine in inflamed joints and serum decreased by the establishment of the AIA model, which was effectively reversed by the
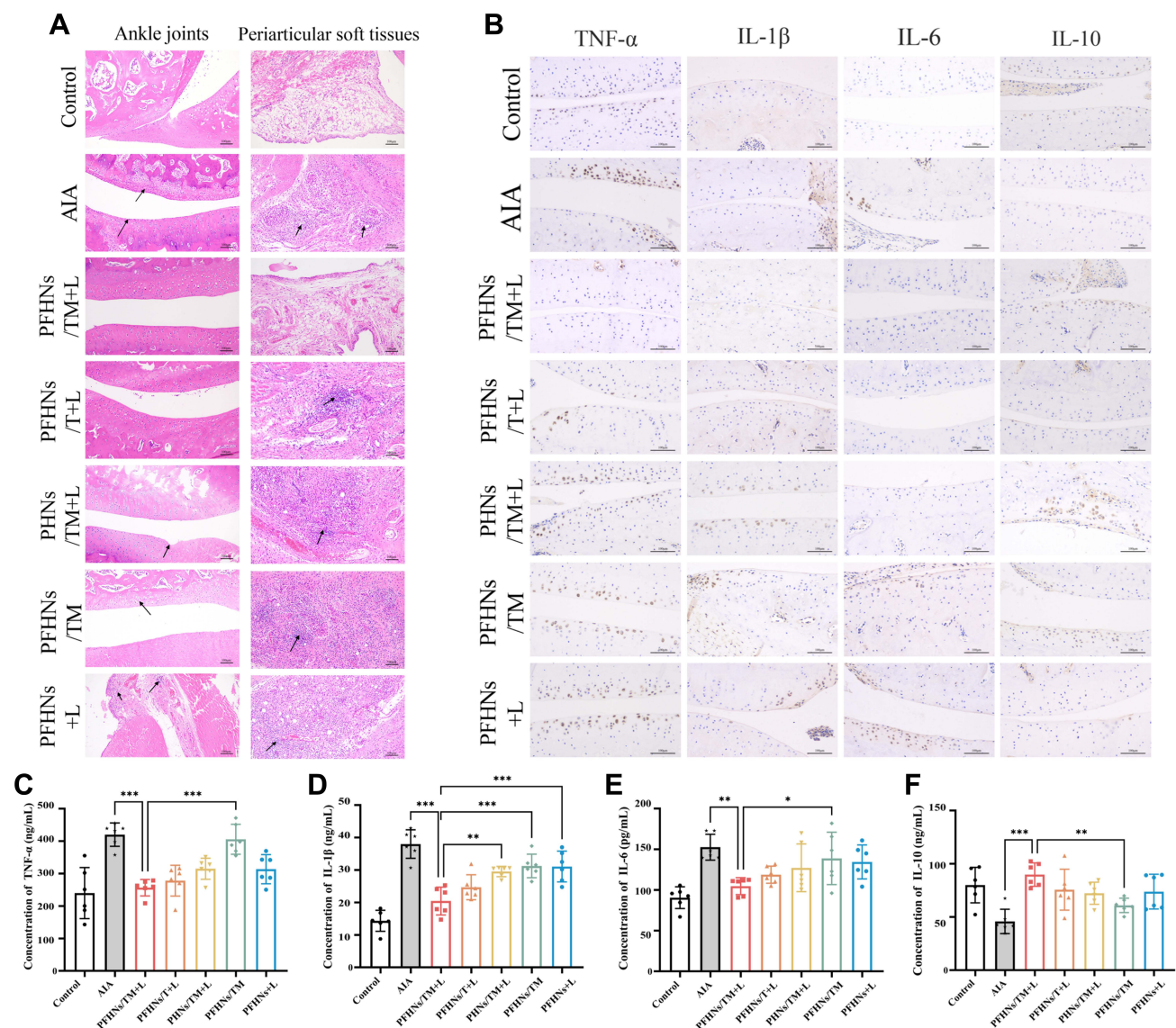

Figure 5 (**A**) H&E staining of rat ankle joints and periarticular soft tissues from different groups of control, AIA, PFHNs/TM+L, PFHNs/T+L, PHNs/TM+L, PFHNs/TM, PFHNs+L. (**B**) Immunohistochemical analysis of rat ankle joints from different groups. Serum concentrations of (**C**) TNF-α, (**D**) IL-1β, (**E**) IL-6, and (**F**) IL-10 (n = 6, *p < 0.05, **p < 0.01, and ***p < 0.001).

treatment with PFHNs/TM+L, whose serum IL-10 concentration was determined to be 89.75 ± 11.03 ng/mL, even higher than the control group (78.48 ± 16.72 ng/mL). The decrease of pro-inflammatory cytokines and the increase in anti-inflammatory cytokines facilitate the inhibition of inflammation.

In addition, H&E staining was used to evaluate the histotoxicity of different formulations to major organs in rats. As shown in Figure S5, no obvious necrosis and damage was observed in the rat major organs from all groups, indicating the good biological safety of all formulations and the method for establishing the AIA rat model.

Overall, PFHNs/TM were efficiently accumulated in the inflamed joints of AIA rats and subsequently killed activated macrophages through NIR-induced combined cytotoxicity of PTT, PDT, HaCT, and apoptosis induced by RNAi, followed by balanced secretion of pro- and anti-inflammatory cytokines, and PFHNs/TM exhibit a good anti-inflammatory effect in vivo.

Conclusion

In summary, we have developed a PCPDTBT-mesoporous silica hybrid nano-delivery system, which is coated with PEI-FA to target activated macrophages for NIR-induced phototherapy, HaCT, and RNAi combined treatment of RA. The prepared PFHNs/TM have high blood compatibility (far below 5% of hemolysis) and ideal in vitro phototherapy properties while controlling the TPZ release and binding of siMcl-1. The large amount of ROS generated by PDT can produce significant toxicity against activated macrophages, and the oxygen consumed on this basis creates a favorable hypoxic environment for TPZ activation. In addition, we prove that PEI-FA-coated PFHNs/TM not only protect the bound siRNA but also are selectively internalized by activated macrophages through FA receptor-ligand-mediated endocytosis, and effectively silence the target anti-apoptotic protein by siMcl-1 transfection. In vivo, PFHNs/TM have also been revealed to be selectively enriched at the inflammatory site of RA, exhibiting NIR-induced combined anti-RA efficacy. In addition, these results also demonstrate the application potential of PFHNs for targeted co-delivery of phototherapeutic agents, chemical drugs, and nucleic acid drugs.

Acknowledgments

Disclosure

The authors report no conflicts of interest in this work.

References

1. Gorantla S, Singhvi G, Rapalli VK, Waghule T, Dubey SK, Saha RN. Targeted drug-delivery systems in the treatment of rheumatoid arthritis: recent advancement and clinical status. *Ther Deliv*. 2020;11(4):269–284. doi:10.4155/tde-2020-0029

2. Bilthariya U, Jain N, Rajoriya V, Jain AK. Folate-conjugated albumin nanoparticles for rheumatoid arthritis-targeted delivery of etoricoxib. *Drug Dev Ind Pharm*. 2015;41(1):95–104. doi:10.3109/03639045.2013.850705

3. Lee SM, Murthy N. Targeted delivery of catalase and superoxide dismutase to macrophages using folate. *Biochem Biophys Res Commun*. 2007;360 (1):275–279. doi:10.1016/j.bbrc.2007.06.054

4. Nogueira E, Gomes AC, Preto A, Cavaco-Paulo A. Folate-targeted nanoparticles for rheumatoid arthritis therapy. *Nanomedi Nanotechnol Biol Med*. 2016;12(4):1113–1126. doi:10.1016/j.nano.2015.12.365

5. Chandrupatla D, Molthoff CFM, Lammertsma AA, van der Laken CJ, Jansen G. The folate receptor as a macrophage-mediated imaging and therapeutic target in rheumatoid arthritis. *Drug Deliv Transl Res*. 2019;9(1):366–378. doi:10.1007/s13346-018-0589-2

6. Mohammadi M, Li Y, Abebe DG, et al. Folate receptor targeted three-layered micelles and hydrogels for gene delivery to activated macrophages. *J Control Release*. 2016;244:269–279. doi:10.1016/j.jconrel.2016.08.020

7. Ge JC, Jia QY, Liu WM, et al. Red-emissive carbon dots for fluorescent, photoacoustic, and thermal theranostics in living mice. *Adv Mater*. 2015;27 (28):4169–4177. doi:10.1002/adma.201500323

8. Jang B, Park JY, Tung CH, Kim IH, Choi Y. Gold nanorod-photosensitizer complex for near-infrared fluorescence imaging and photodynamic/ photothermal therapy in vivo. *Acs Nano*. 2011;5(2):1086–1094. doi:10.1021/nn102722z

9. Gulzar A, Xu JT, Yang D, et al. Nano-graphene oxide-UCNP-Ce6 covalently constructed nanocomposites for NIR-mediated bioimaging and PTT/ PDT combinatorial therapy. *Dalton Trans*. 2020;49(26):9164–9165. doi:10.1039/D0DT90115F

10. Bian H, Ma DD, Zhang XF, et al. Tailored engineering of novel xanthonium polymethine dyes for synergetic PDT and PTT triggered by 1064 nm laser toward deep-seated tumors. *Small*. 2021;17(21):2100398. doi:10.1002/smll.202100398

11. Li Z, Wu XN, Gu WX, et al. Photogenerated electrons from CeO$_2$ via upconversion of excitons to conduction band enhanced photocatalysis for photo-therapy of rheumatoid arthritis. *Chem Eng J*. 2022;446(1):136904. doi:10.1016/j.cej.2022.136904

12. Zhang WS, Deng WX, Zhang H, et al. Bioorthogonal-targeted 1064 nm excitation theranostic nanoplatform for precise NIR-IIa fluorescence imaging guided efficient NIR-II photothermal therapy. *Biomaterials*. 2020;243:119934. doi:10.1016/j.biomaterials.2020.119934

13. Wu XZ, Suo YK, Shi H, et al. Deep-tissue photothermal therapy using laser illumination at NIR-IIa window. *Nano Micro Lett*. 2020;12(1):38. doi:10.1007/s40820-020-0378-6

14. Pan WZ, Li Z, Qiu S, et al. Octahedral Pt-MOF with Au deposition for plasmonic effect and Schottky junction enhanced hydrogenothermal therapy of rheumatoid arthritis. *Materials Today Bio*. 2022;13:100214. doi:10.1016/j.mtbio.2022.100214

15. Lin HX, Lin ZX, Zheng KH, et al. Near-infrared-II nanomaterials for fluorescence imaging and photodynamic therapy. *Adv Opt Mater*. 2021;9(9):2002177. doi:10.1002/adom.202002177

16. Li JC, Zhen X, Lyu Y, Jiang YY, Huang JG, Pu KY. Cell membrane coated semiconducting polymer nanoparticles for enhanced multimodal cancer phototheranostics. *Acs Nano*. 2018;12(8):8520–8530. doi:10.1021/acsnano.8b04066

17. Yuan Y, Diao SC, Ni XY, et al. Peptide-based semiconducting polymer nanoparticles for osteosarcoma-targeted NIR-II fluorescence/ NIR-I photoacoustic dual-model imaging and photothermal/photodynamic therapies. *J Nanobiotechnology*. 2022;20(1):44. doi:10.1186/s12951-022-01249-4

18. Chen WH, Luo GF, Qiu WX, et al. Mesoporous silica-based versatile theranostic nanoplatform constructed by layer-by-layer assembly for excellent photodynamic/chemo therapy. *Biomaterials*. 2017;117:54–65. doi:10.1016/j.biomaterials.2016.11.057

19. Liu YY, Liu Y, Bu WB, et al. Hypoxia induced by upconversion-based photodynamic therapy: towards highly effective synergistic bioreductive therapy in tumors. *Angew Chem Int Ed Engl*. 2015;54(28):8105–8109. doi:10.1002/anie.201500478

20. Huang RQ, Zhang CY, Bu YY, et al. A multifunctional nano-therapeutic platform based on octahedral yolk-shell Au NR@CuS: photothermal/ photodynamic and targeted drug delivery tri-combined therapy for rheumatoid arthritis. *Biomaterials*. 2021;277:121088. doi:10.1016/j.biomaterials.2021.121088

21. Shih CY, Wang PT, Su WC, Teng HS, Huang WL. Nanomedicine-based strategies assisting photodynamic therapy for hypoxic tumors: state-of-the-art approaches and emerging trends. *Biomedicines*. 2021;9(2):137. doi:10.3390/biomedicines9020137

22. Cheng D, Ji YJ, Wang B, et al. Enzyme/GSH dual-responsive biodegradable nanohybrid for spatiotemporally specific photodynamic and hypoxia-augmented therapy against tumors. *Int J Pharm*. 2021;603:120730. doi:10.1016/j.ijpharm.2021.120730

23. Dong YX, Zhou L, Shen ZJ, et al. Iodinated cyanine dye-based nanosystem for synergistic phototherapy and hypoxia-activated bioreductive therapy. *Drug Deliv*. 2022;29(1):238–253. doi:10.1080/10717544.2021.2023701

24. Shao YL, Liu B, Di ZH, et al. Engineering of upconverted metal-organic frameworks for near-infrared light-triggered combinational photodynamic/ chemo-/immunotherapy against hypoxic tumors. *J Am Chem Soc*. 2020;142(8):3939–3946. doi:10.1021/jacs.9b12788

25. Bollu A, Hassan MK, Dixit M, Sharma NK. The 2 '-caged-tethered-siRNA shows light-dependent temporal controlled RNAi activity for GFP gene into HEK293T cells. *Bioorg Med Chem*. 2021;301:15932.

26. Chiu YL, Ali A, Chu CY, Cao H, Rana TM. Visualizing a correlation between siRNA localization, cellular uptake, and RNAi in living cells. *Chem Biol*. 2004;11(8):1165–1175. doi:10.1016/j.chembiol.2004.06.006

27. Chen MY, Dong CY, Shi S. Nanoparticle-mediated siRNA delivery and multifunctional modification strategies for effective cancer therapy. *Adv Mater Technol*. 2021;6(10):2001236. doi:10.1002/admt.202001236

28. He SF, Fan WW, Wu N, et al. Lipid-Based liquid crystalline nanoparticles facilitate cytosolic delivery of siRNA via structural transformation. *Nano Lett*. 2018;18(4):2411–2419. doi:10.1021/acs.nanolett.7b05430

29. Sivakumar P, Kim S, Kang HC, Shim MS. Targeted siRNA delivery using aptamer-siRNA chimeras and aptamer-conjugated nanoparticles. *Wiley Interdiscip Rev Nanomed Nanobiotechnol*. 2019;11(3):e1543. doi:10.1002/wnan.1543

30. Hobel S, Appeldoorn CCM, Gaillard PJ, Aigner A. Targeted CRM197-PEG-PEI/siRNA complexes for therapeutic RNAi in glioblastoma. *Pharmaceuticals*. 2011;4(12):1591–1606. doi:10.3390/ph4121591

31. Shim MS, Chang SS, Kwon YJ. Stimuli-responsive siRNA carriers for efficient gene silencing in tumors via systemic delivery. *Biomaterial Sci*. 2014;2(1):35–40. doi:10.1039/C3BM60187K

32. Liu HT, Huang QQ, Shi B, Eksarko P, Temkin V, Pope RM. Regulation of Mcl-1 expression in rheumatoid arthritis synovial macrophages. *Arthritis Rheum*. 2006;54(10):3174–3181. doi:10.1002/art.22132

33. Li XY, Zhang SX, Zhang XY, et al. Folate receptor-targeting semiconducting polymer dots hybrid mesoporous silica nanoparticles against rheumatoid arthritis through synergistic photothermal therapy, photodynamic therapy, and chemotherapy. *Int J Pharm*. 2021;607:120947. doi:10.1016/j.ijpharm.2021.120947

34. Li G, Xu F, Yang B, et al. A nanotherapy responsive to the inflammatory microenvironment for the dual-targeted treatment of atherosclerosis. *Nanomedicine*. 2022;43:102557. doi:10.1016/j.nano.2022.102557